The Marine-Atmospheric Emitted Radiance Interferometer: A High-Accuracy, Seagoing Infrared Spectroradiometer

P. J. MINNETT

Division of Meteorology and Physical Oceanography, Rosenstiel School of Marine and Atmospheric Science, University of Miami, Miami, Florida

R. O. KNUTESON AND F. A. BEST

Space Science and Engineering Center, University of Wisconsin—Madison, Madison, Wisconsin

B. J. OSBORNE*

School of Physical Sciences, Curtin University of Technology, Perth, Western Australia

J. A. HANAFIN AND O. B. BROWN

Division of Meteorology and Physical Oceanography, Rosenstiel School of Marine and Atmospheric Science, University of Miami, Miami, Florida

(Manuscript received 14 January 2000, in final form 8 November 2000)

ABSTRACT

The Marine-Atmospheric Emitted Radiance Interferometer (M-AERI) is described, and some examples of the environmental variables that can be derived from its measurements and the types of research that these can support are briefly presented. The M-AERI is a robust, accurate, self-calibrating, seagoing Fourier-transform interferometric infrared spectroradiometer that is deployed on marine platforms to measure the emission spectra from the sea surface and marine atmosphere. The instrument works continuously under computer control and functions well under a very wide range of environmental conditions with a high rate of data return. Spectral measurements are made in the range of ~3 to ~18 μm wavelength and are calibrated using two internal, National Institute of Standards and Technology–traceable blackbody cavities. The environmental variables derived from the spectra include the surface skin temperature of the ocean, surface emissivity, near-surface air temperature, and profiles of temperature and humidity through the lower troposphere. These measurements are sufficiently accurate both to validate satellite-derived surface temperature fields and to study the physics of the skin layer.

1. Introduction

There is growing recognition in the oceanographic community that temperature gradients in the uppermost few millimeters of the ocean have more than simple curiosity value, but have significant consequences in a number of applications of sea surface temperature (SST) measurements. Such applications range from the studies of air–sea heat and gas transfer, which operate on the microscale, to the compilation of SST fields derived from satellite measurements, which require global-scale datasets. The air–sea heat exchange, comprising radiative, latent, and sensible components, is both the cause and result of these near-surface temperature gradients, often referred to as the ''skin effect'' (Fig. 1). Typically, the temperature of the ocean, measured in the bulk of the fluid close to the surface, is greater than the bulk air temperature above, resulting in a heat flow from the ocean to atmosphere. Both above and below the air–sea interface, the heat flow can be efficiently accommodated by turbulent transfer. At the interface itself, turbulence is inhibited by the great density contrast between air and water, giving rise to a ''skin'' layer, where heat flow is primarily the result of molecular conduction and electromagnetic radiation. These processes are less efficient at transferring heat, with the result that a vertical temperature gradient exists such that the temperature at the top of the skin layer is generally cooler than the tem-

* Current affiliation: Space Science and Engineering Center, University of Wisconsin—Madison, Madison, Wisconsin.

Corresponding author address: P. J. Minnett, Division of Meteorology and Physical Oceanography, Rosenstiel School of Marine and Atmospheric Science, University of Miami, 4600 Rickenbacker Causeway, Miami, FL 33149.
E-mail: pminnett@rsmas.miami.edu

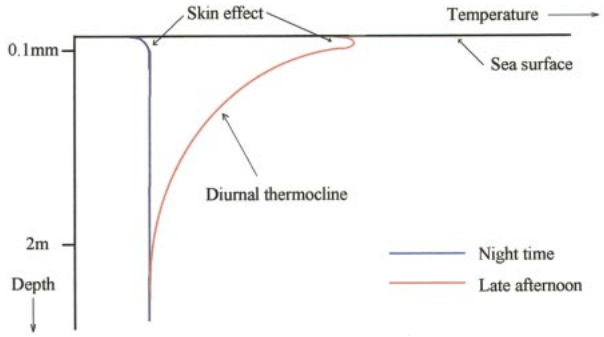

FIG. 1. Sketch of the vertical temperature gradients at the surface of the ocean.

perature in the near-surface layer underneath. Whenever there is net heat flux between the ocean and atmosphere, the skin effect is present.

The skin effect has been the subject of attention over several decades; for a recent review, please see Wick et al. (1996). Renewed interest in skin temperature measurements has been stimulated, at least in part, by the need to validate satellite-derived SST fields. Variability in the SST caused by the skin effect is a significant contributor to the residual uncertainty of validations made using in situ bulk temperatures (Kearns et al. 2000), and this uncertainty is conventionally ascribed to inaccuracies in the satellite-based measurement. The need to improve the error budget of global, satellite-derived SST fields requires the use of accurate skin temperature measurements in the validation procedures.

One possible reason that the skin layer has received relatively little attention since the earlier work in the 1970s is the difficulty of establishing that the measurements of the skin temperature are sufficiently accurate to study the effect. The drop in temperature across the skin layer is generally only a few tenths of a degree Celsius, and it is difficult to demonstrate convincingly that either in situ or radiometric measurements are accurate enough to resolve the gradients. The in situ measurements are made by rapid-response microthermometers, and here the problem is two-fold: resolving the submillimeter scale gradients and demonstrating calibration accuracy. Infrared radiometric measurements of the skin layer are often compromised by the difficulty of maintaining absolute calibration accuracy and of correcting for the effects of the reflected sky radiation.

Published reports on in situ profiling of the skin layer show that such measurements are possible in the laboratory (Katsaros et al. 1977) and in the field (Mammen and von Bosse 1990), but such datasets are few and taken under a limited range of conditions. There are more examples of investigations of the skin effect using infrared radiometry to measure the skin temperature (e.g., Schluessel et al. 1987; Donlon and Robinson 1997), and these encompass a wider range of conditions. But in many of these, the accuracy of the radiometric measurement is comparable to the size of the effect being studied. Those datasets that rely on internal calibration of the radiometers have stated accuracies of about 0.1 K. Others (e.g., Schluessel et al. 1987) that use a separate, well-stirred water bath with in situ thermometers, for which the calibration may have uncertainties of <0.01 K, rely on the presumption that the skin layer is destroyed, so the bulk temperature measurement corresponds to that measured radiometrically. The small component of reflected sky radiance in the radiometer measurement is another source of uncertainty that is present in radiometric measurements, whether calibrated internally or with a water bath. In the former case, direct measurements of the downwelling sky radiance are needed for an explicit correction. When the sky is clear and dry, this requires a large dynamic range of the radiometer and its calibration; and in cases of broken cloud, the assumption must be made that the sky radiance measurement is the same as is reflected at the sea surface. For measurements calibrated using the stirred water-bath method, the assumption is made that the sky radiation reflected from the surface of the water bath corresponds to that reflected at the sea surface.

This paper describes a new instrument that is capable of making skin temperature measurements with absolute accuracies inferred to be better than 0.1 K in the field in a wide range of conditions. This instrument, the Marine-Atmospheric Emitted Radiance Interferometer (M-AERI), has been used on several research cruises. Examples of data from some of these cruises are included here along with laboratory data to demonstrate the radiometric accuracy of the M-AERI measurements. The M-AERI SSTs are being used to validate satellite-derived SST retrievals (Smith et al. 1996; Kearns et al. 2000) and to study the physical processes that determine the size of the thermal skin effect.

2. The M-AERI

The M-AERI is a seagoing development of the Atmospheric Emitted Radiance Interferometer (AERI), an instrument developed at the Space Science and Engineering Center (SSEC) at the University of Wisconsin—Madison for the Department of Energy Atmospheric Radiation Measurement Program (Stokes and Schwartz 1994), and of the airborne High-Resolution Interferometer Sounder (HIS), which has been flown on the National Aeronautics and Space Administration (NASA) ER-2 research aircraft (Revercomb et al. 1988).

At the time of this writing (August 2000), M-AERIs have been used on 15 research cruises on 10 different vessels. These are in addition to the proof-of-concept experiment, which lasted a few days in the Gulf of Mexico, which has been reported by Smith et al. (1996), and a one-day acceptance test in inshore Floridian waters. These cruises include 4 in the Arctic and 7 in equatorial conditions and have ranged from about 10 days to 4½ months duration. On no occasion has data collection been terminated by an instrument failure.

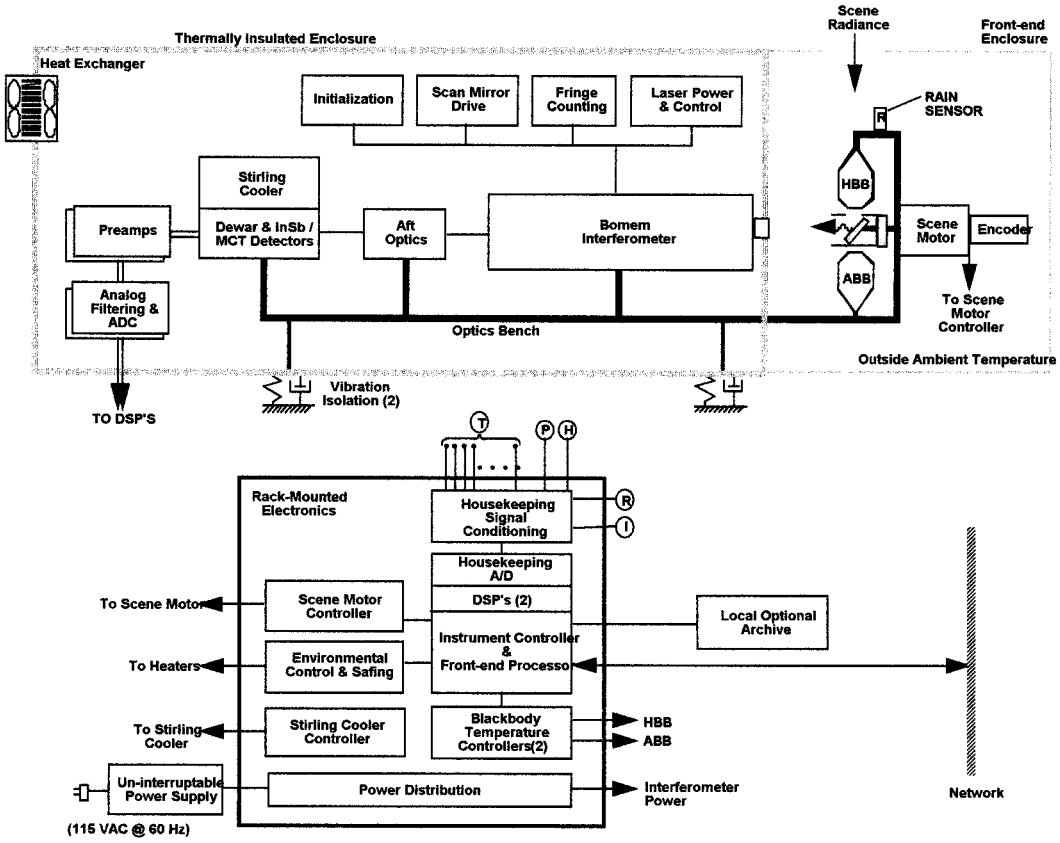

FIG. 2. Schematic diagram of the components of the M-AERI.

a. Overview

The M-AERI system consists of two main components: an external unit that is mounted on the deck of the ship and an electronics rack that is installed inside the vessel, the two being linked by an umbilical cable up to 60 m in length. The external unit comprises the Fourier transform infrared (FTIR) interferometer assembly (Griffiths and de Haseth 1986) with detectors, a detector cooler, an optics chamber, calibration cavities, a scan mirror and motor, and ancillary sensors. The rack of electronics includes the computer for instrument control and data acquisition, processing and display, the interfaces and control units for the scan mirror, blackbodies, the detector cooler, and power conditioning units (Fig. 2). A global positioning system (GPS) antenna is mounted externally. Because of the difficulties of effective grounding on a ship and the likelihood of ''ground-loops,'' all of the equipment shares a common ground through the chassis of the electronics rack. In the majority of cases of shipboard use, it has been necessary to include an isolating transformer between the ship's power supply and the M-AERI uninterruptible power supply (UPS).

The FTIR spectrometer operates in the range of infrared wavelengths from $\sim$3 to $\sim$18 μm and measures spectra with a resolution of $\sim$0.5 cm^{-1}. Figure 3 shows part of temperature spectra measured at different view angles by the M-AERI while directed at the sky (top) and sea surface (bottom). This spectral range includes the intervals where satellite-borne infrared radiometers measure the SST in the so-called atmospheric windows where the transmission is high. The Advanced Very High Resolution Radiometer (AVHRR), the Along Track Scanning Radiometer (ATSR) (Mutlow et al. 1994; Minnett 1995), and the Moderate Resolution Imaging Spectroradiometer (MODIS; Esaias et al. 1998) all have two channels in the spectral region from about 800 to 1000 cm^{-1} (λ = 10–12.5 μm). In Fig. 3, the spectral intervals where the sky temperatures are smallest indicate where the atmosphere is most transparent. As the view angle moves away from zenith, the atmospheric spectra in the transmissive regions become warmer as the path length traverses lower, and therefore warmer, portions of the atmosphere. Emission lines of the gaseous atmospheric constituents cause the spikes in the atmospheric spectra, and the slope at the base of these lines, in the 800- to 1000-cm^{-1} interval, is caused by the anomalous continuum emission of water vapor. If the sea surface were a perfect blackbody, the water view would be a smooth line at the skin temperature, but the small departure from unity in the emissivity of the sea surface results in reflection of the sky radiance

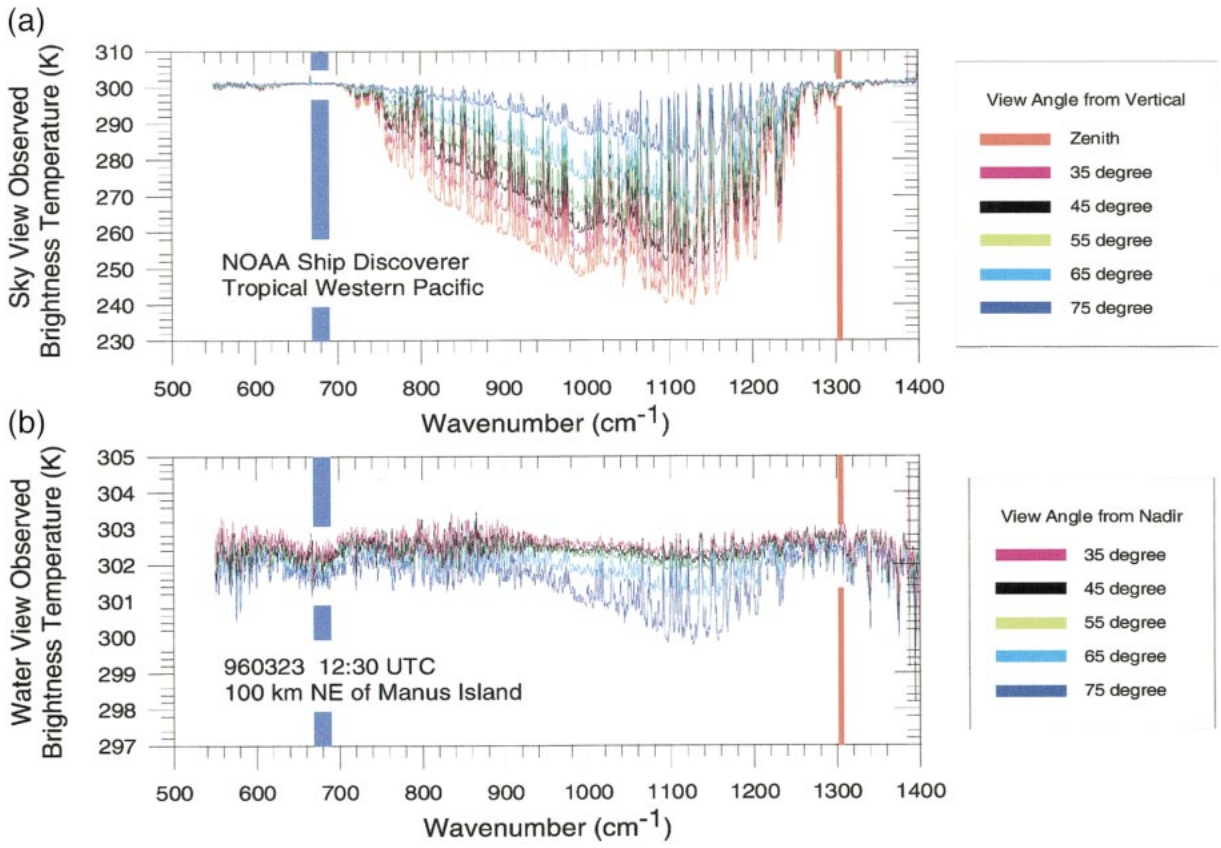

FIG. 3. Examples of parts of spectra measured by the M-AERI while directed at the sky (top) and sea surface (bottom) at a range of angles (measured from zenith for the sky and nadir for the ocean). The spectra are represented as temperature, and those intervals where the sky temperatures are smallest indicate where the atmosphere is most transparent. The spikes in the atmospheric spectra are caused by emission lines. The small departure from unity in the emissivity of the sea surface results in reflection of the sky radiance in the sea-viewing measurement, including the atmospheric emission lines. The blue bar shows which spectral region is used to measure air temperature and the red bar skin sea-surface temperature. Note the change in temperature scales of the two panels. These data were taken in the tropical western Pacific during the Combined Sensor Program Cruise in 1996 (Post et al. 1997).

in the sea-viewing measurement, including the atmospheric emission lines. The retrieval of SST from these spectra requires the correction of the reflected radiance (see section 4a below).

The M-AERI uses two infrared detectors to achieve this wide spectral range, and these are cooled to ~78 K (i.e., close to the boiling point of liquid nitrogen) by a Stirling cycle mechanical cooler to reduce the noise equivalent temperature difference to levels well below 0.1 K. The M-AERI includes two internal blackbody cavities for accurate real-time calibration (see section 2f2 below). The scan mirror is programmed to step through a preselected range of angles, directing the field of view of the interferometer to either of the blackbody calibration targets or to the environment from nadir to zenith. The interferometer integrates measurements over a preselected time interval, usually a few tens of seconds, to obtain a satisfactory signal-to-noise ratio. A typical operational cycle, including 2 view angles to the atmosphere, 1 to the ocean, and 2 calibration measurements, takes about 5 min. Table 1 summarizes the key instrument parameters of a M-AERI system.

b. Components

The heart of the M-AERI is the MR-100 series FTIR interferometer (Griffiths and de Haseth 1986) manufactured in Canada by Bomem Inc.[1] This is a self-contained unit in a hermetically sealed cast aluminum housing with approximate dimensions 20 cm high, 55 cm long, and 50 cm wide and weighing about 45 kg. The case contains an interferometer subassembly, an integrated helium–neon (HeNe) laser used for sample triggering, and associated support electronics to provide power and analog-to-digital signal conversion. The MR-100 provides digital sample points through a serial port con-

[1] The use of company and product names does not imply endorsement of these products by the publisher of this article or by the agencies that funded this work.

TABLE 1. Characteristics of the M-AERI.

Interferometer	Bomem MR-100 type Patented Michelson wishbone design Two input and two output beams Two cube-corner retroreflectors KBr beam-splitter with ZnSe windows
Nominal beam diameter	2.5 cm
Fringe counting	Single fringe sampling, continuous
Optical path drive	Voice coil drive, flex pivot rotation
Maximum optical path difference	± 1.037 cm^{-1}
Optical path difference sampling reference	HeNe Laser with white light at startup
Scan time	1 s (in each direction)
Raw data rate	32 768 (16 bit) samples s^{-1}
Spectral coverage:	
Long wave ((HgCdTe)	5.5–18.2 μm, 550–1800 cm^{-1}
Short wave (InSb)	3.3–5.5 μm, 1800–3000 cm^{-1}
Spectral sampling	0.48 cm^{-1}
Instrument field-of-view	45 mrad (full angle)
Entrance aperture	6.9 cm (2.7 in) at blackbodies
Dwell time per scene	Programmable, typically 45 s
Cooler; Temperature	0.6 W Stirling Cooler (Litton); 78 K
Rms noise (per scene), NEΔL	$<$0.2 mW (m^2 sr cm^{-1})$^{-1}$ (670–1400 cm^{-1}) $<$0.015 mW (m^2 sr cm^{-1})$^{-1}$ (2000–2600 cm^{-1})
Onboard calibration	Two high emissivity cavities ($>$0.996) HBB controlled to 60°C ABB at environmental temperature
Radiometric calibration	$<$0.05 K at ambient, absolute $<$1% of ambient radiance, all scenes
Dimensions (excluding electronics rack)	116 cm L $\times$ 71 cm W $\times$ 76 cm H
Mass (excluding electronics rack)	93 kg
Power (system)	1 kW (approx.)

nection to a PC-based digital signal processor card where the measured interferogram is Fourier transformed to the spectral domain. The system operates at an output rate of 1 interferogram (or complex spectrum) per second.

The interferometer subassembly consists of a patented Michelson-type interferometer with two corner-cube retroreflectors mounted on a ''wishbone'' swing arm with flex pivot rotation. A voice coil actuator drives the wishbone with precise velocity control via the reference laser fringes. A beam-splitter is oriented such that the rotary scanning motion simultaneously increases the optical path in one arm of the interferometer and reduces it in the other. The maximum optical path difference is 1 cm on both sides of the center burst (zero path difference). The interferometer design makes the system relatively immune to vibration-induced spectral artifacts, an important consideration for shipboard operation.

A field stop defines the instrument field of view, which is also the interferometer field of view, since there is no telescope on the M-AERI system, and for the FTIR to be used as a radiometer, the aft optics images the field stop on the detectors. This is important to obtain nonweighted average radiometric readings from nonhomogeneous sources such as partly cloudy sky scenes. A ''sandwich'' of two detectors is used, indium antimonide (InSb) in front of mercury cadmium telluride (HgCdTe). The InSb detector is for the so-called short-wave part of the spectrum from about 1800 to 3000 cm^{-1} (3.3–5.5 μm) and the HgCdTe detector for the long-wave part from about 550 to 1800 cm^{-1} (5.5–18 μm). The detectors are continuously cooled to the operating temperature of $\sim$78 K by a mechanical Stirling cycle cooler, manufactured by Litton Life Support Systems Inc., which uses helium as the working fluid. No liquid nitrogen (or other cryogen) is required for the operation of the M-AERI system, an important advantage for operations at sea.

The MR-100 has two entrance ports and one useable exit port in the sealed case containing the interferometer beam splitter. The potassium bromide (KBr) beam splitter is hygroscopic and requires the internal case humidity to remain below 30% RH to prevent permanent damage. The exit port of the M-AERI is a ZnSe window in the top of the interferometer case that allows the output of the interferometer to be directed into the aft optics and eventually onto the detector package. The second of the two entrance ports on the M-AERI system is sealed with a massive copper plug to provide a stable reference during a calibration cycle. The primary entrance port is another ZnSe window that is open to the outside air. There has been no evidence during cruises of condensation occurring on the window, a result of the slightly elevated temperature of the window with respect to the surrounding structure caused by the heat generated within the interferometer. The external window coatings are designed to be immune to corrosive hazing or fogging caused by the marine atmosphere. This is an important consideration for a system intended for operation in the environment near the ocean surface.

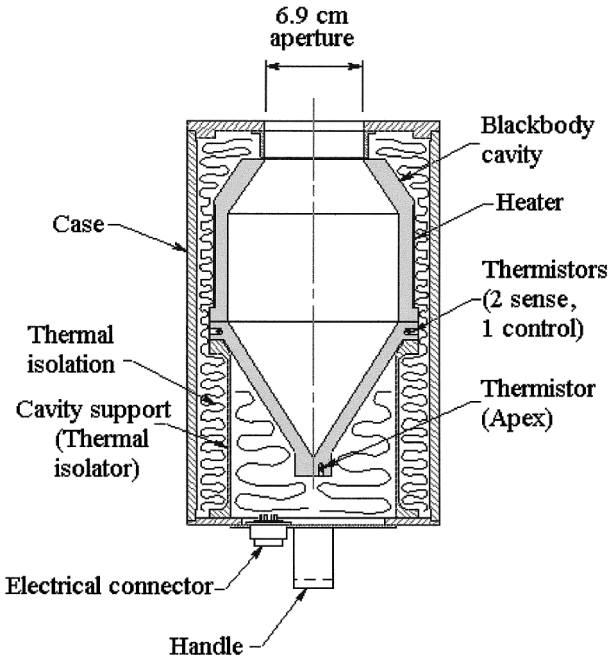

FIG. 4. Diagram of an M-AERI blackbody cavity. Two such cavities are used in the routine calibration of the measurements; one being heated to 60°C and the other floating close to ambient temperatures. To validate the calibration, a third cavity is attached to the instrument at the position of the zenith view, the temperature of which can be programmed to a number of set points spanning the SST range.

The MR-100 is aligned to an optics bench containing the reference blackbodies (Fig. 4) used by the M-AERI system for routine calibration. The blackbody cavities are copper cylinders with conical end plates, one with a circular orifice to allow the radiation to emerge. The internal walls are painted matte black (Chemglaze Z306 Urethane Coating), and the cavity has an effective emissivity of 0.996, with an uncertainty of 0.001. This paint produces a diffuse (lambertian) finish as opposed to specular, and while the more internal reflections supported by a specular paint can, in principle, lead to a high cavity emissivity, the surface is prone to contamination at sea by salt microcrystals from marine aerosols. This would lead to an uncharacterized change in emissivity by introducing diffuse scattering elements on the paint surface. A lambertian finish on the cavity walls is largely immune to this effect. A ray-tracing study has shown that 81% of the emergent radiation originates from the conical base and the remainder from the sidewalls. There are heating coils wrapped around the cylindrical walls toward the open end of the cavity, and three thermistors are used to measure its temperature. One thermistor is fixed at the apex of the base, and the other two are diametrically opposite each other close to the top of the conical base. Two blackbodies are fixed to the hexagonal structure that supports the scan mirror motor, with their axes at 60° and 120° to the vertical. The upper one is heated to 60°C, and the lower one floats at ambient temperature. The temperature measured by the 3 thermistors in the ambient temperature cavity agree to ~0.01 K, whereas the apex temperature of the hot target may be up to ~0.2 K warmer than at the aperture, an effect that results from some conductive heat loss through the neck of the cavity. During construction, the blackbody thermistors are calibrated against thermometers traceable to National Institute of Standards and Technology (NIST) standards to better than 0.05 K.

TABLE 2. Housekeeping variables.

Channel number	Variable
00	Temperature at top of ambient-temperature blackbody calibration target
01	Temperature at apex of ambient-temperature blackbody calibration target
02	Temperature at bottom of ambient-temperature blackbody calibration target
03	Temperature at top of hot blackbody calibration target
04	Temperature at apex of hot blackbody calibration target
05	Temperature at bottom of hot blackbody calibration target
06	Fixed 2500 Ω resistor
07	Fixed 97 kΩ resistor
08	Air temperature outside M-AERI enclosure
09	Air temperature near interferometer
10	Interferometer second port temperature
11	Temperature of the support structure of the blackbody targets
12	Air temperature near blackbody targets
13	Mirror motor temperature
15	Fixed 12 kΩ resistor
16	No. 1. Blackbody controller temperature
17	No. 2. Blackbody controller temperature
18	Cooler compressor temperature
19	Cooler expander temperature
20	Cooler power supply temperature
21	Ambient temperature of electronics rack
22	Temperature of control computer housing
23	Motor driver temperature
24	SCE (sensor conditioning electronics unit) temperature
25	Cooler current
26	Detector temperature
27	Rainfall intensity
28	Interferometer window temperature
31	Spare thermometer (measures air temperature inside M-AERI enclosure)
32	Atmospheric relative humidity
33	Interferometer enclosure relative humidity
34	Atmospheric pressure
1024	Pitch angle of optical bench (digital channel)
1025	Roll angle of optical bench (digital channel)

The M-AERI includes a variety of sensors used, ensuring the calibration of the spectra, monitoring the state of the instrument, and measuring relevant environmental parameters (Table 2), which are recorded every 5 s. Each of the blackbody calibration targets has four thermistors, the values of which are digitized at the electronics interface at the internally mounted rack. Three of these are used to measure the temperature of the cavity and

the fourth in the temperature control circuitry. To account for possible changes in the resistance of the cables connecting the thermistors to the digitizers (or within the digitizing circuitry itself) that could invalidate the calibration of the spectra, the values of three fixed-value precision resistors, mounted at the external unit, are monitored. The internal relative humidity is monitored for instrument safety as is the relative humidity in the area surrounding the blackbody cavities. The rainfall measurement is used in the mirror safe-mode procedure (see 2c below). The majority of the other sensors are there to provide information to diagnose situations that might lead to degradation in the data quality.

The optical components of the M-AERI are firmly mounted onto a rigid optical bench, which is mounted through shock absorbers onto the instrument baseplate. This in turn is shock-mounted onto an instrument table, which has individually telescoping legs that are used to compensate for the slope of the deck to make the table level. The legs are securely fixed to the deck and railing of the ship. Figure 5 shows the M-AERI external unit mounted on the National Oceanic and Atmosphere Administration (NOAA) Ship *Ronald H. Brown.*

The M-AERI is equipped with pitch and roll sensors so that the influence of the ship's motion on the measurements can be determined; large rolls may bring the field of view into the influence of the bow wave and change the angle of incidence at the sea surface thereby changing the emissivity (and reflectivity) in the field of view. It is current practice to include a television camera in the M-AERI shipboard installation to monitor the field of view of the M-AERI sea-directed measurement. The imagery is stored on a time-lapse video recorder for later analysis to identify periods when the data may be contaminated by the influence of the ship's bow wave.

The control computer is an Industrial Computer Sources PC with a 166 MHz Intel Pentium processor running an IBM OS/2 operating system. This shares a half-height rack with the control electronics units for the calibration cavities, the detector coolers, the scan mirror controller, the sensor interface electronics, and the GPS receiver. The real-time data display is designed to provide a graphical representation of not only the spectral data but also instrument metadata that serves to alert the operator to anomalous situations that may compromise the quality of the data. In addition to the spectral measurements from each detector, which are refreshed each time a new spectrum is computed, selected variables are displayed as time series while others are displayed using a ''traffic-light'' code in a matrix of ''warning lights'' (Fig. 6).

c. Operations

The M-AERI runs continuously under computer control, except for a brief period beginning at 0000 UTC, when the computer reboots and undertakes some housekeeping tasks. These include ensuring there is enough disk space for the new day's measurements. If the available disk space is too small, the oldest day's data are deleted; so to avoid data loss, the operator must backup the previous day's measurements to an archive medium. While causing a small (several minutes) loss of data, the daily reboot serves to identify and rectify any residual problems that may have resulted from anomalous situations in the instrument, computer, or software that may not be apparent to the operator and that may eventually lead to a system crash or loss of data.

The most serious source of data loss results from the measures taken to avoid contamination of the scan mirror by heavy rain or sea spray. The mirror must remain clean and dry for the M-AERI to provide the required measurements. Contaminants on the mirror, wet or dry, act as irregularities that scatter stray radiation into the beam. The sources of these strays are not characterized and not necessarily the same for the sky and sea measurements. They are not likely to be the same for the calibration measurements of the blackbody cavities, so their influence is not necessarily removed by the real-time calibration procedure. To avoid such contamination, a rain sensor (Väisälä type DRD11-A) is mounted close to the M-AERI aperture, and when the output from this crosses a predetermined threshold, the mirror is moved into a ''safe'' position. The mirror is enclosed in a metal cylinder with a circular aperture in the side for the field of view, which rotates with the mirror, protecting it from light spray. In the safe mode, the mirror surface is directed to the lower, ambient-temperature, blackbody calibration cavity, and the back of the mirror cylinder is presented to the rain or spray. When the rain sensor output recovers through the threshold value again, the mirror scan sequence is resumed. The rain sensor is not used to measure rain rate, a notoriously difficult measurement from a ship, but merely to indicate the presence of rain or spray. The threshold for ''safing'' is set very low so that the mirror is ''safed'' when only one or two water droplets are detected on the 7.2 cm^2 area of the sensor. The sensing element must be kept clean to ensure reliable operation and to help counteract the effects of calibration drift (which, on some occasions, requires periodic resetting of the threshold values). There is the option of an operator override of the automatic mirror safing mechanism, which causes the mirror to immediately enter or exit the safe mode. When the risk of salt spray entering the instruments is high, and during heavy rain, the M-AERI is covered for protection, and no useful data are collected. Similarly, when there is evidence of direct sunlight entering the aperture, a shield is used that obscures some of the environmental views at the affected mirror angles. A typical example of the rate of data return is given in Fig. 7 for a deployment of 57 days in the North Atlantic Ocean in summer 1998. Data loss by maintenance, mirror ''safing,'' and instrumental problems constitute 6.4% of the maximum possible data return. Fur-

FIG. 5. The M-AERI installed on the NOAA S *Ronald H. Brown.* The instrument is on the forward 02 deck at the starboard railing. The field of view intersects the sea surface ahead of the bow wave.

ther loss of data caused by covering the instrument in heavy rain and spray resulted in a return rate of 78% of the maximum possible.

d. Data flow

As shown in Fig. 2, the M-AERI computer has an interface to each of the instrument subsystems. In particular, data are routinely collected from the MR-100 interferometer through a digital signal processing card in the computer, which performs a fast Fourier transform (FFT) in real time (1-s intervals). The interferometer data are merged with a comprehensive set of housekeeping data collected from the blackbody subsystem, the mirror controller, the environmental monitors (temperature, humidity, pressure, and precipitation), a GPS location and time, and an inclinometer. The housekeeping data are sampled and recorded at 5-s intervals (200

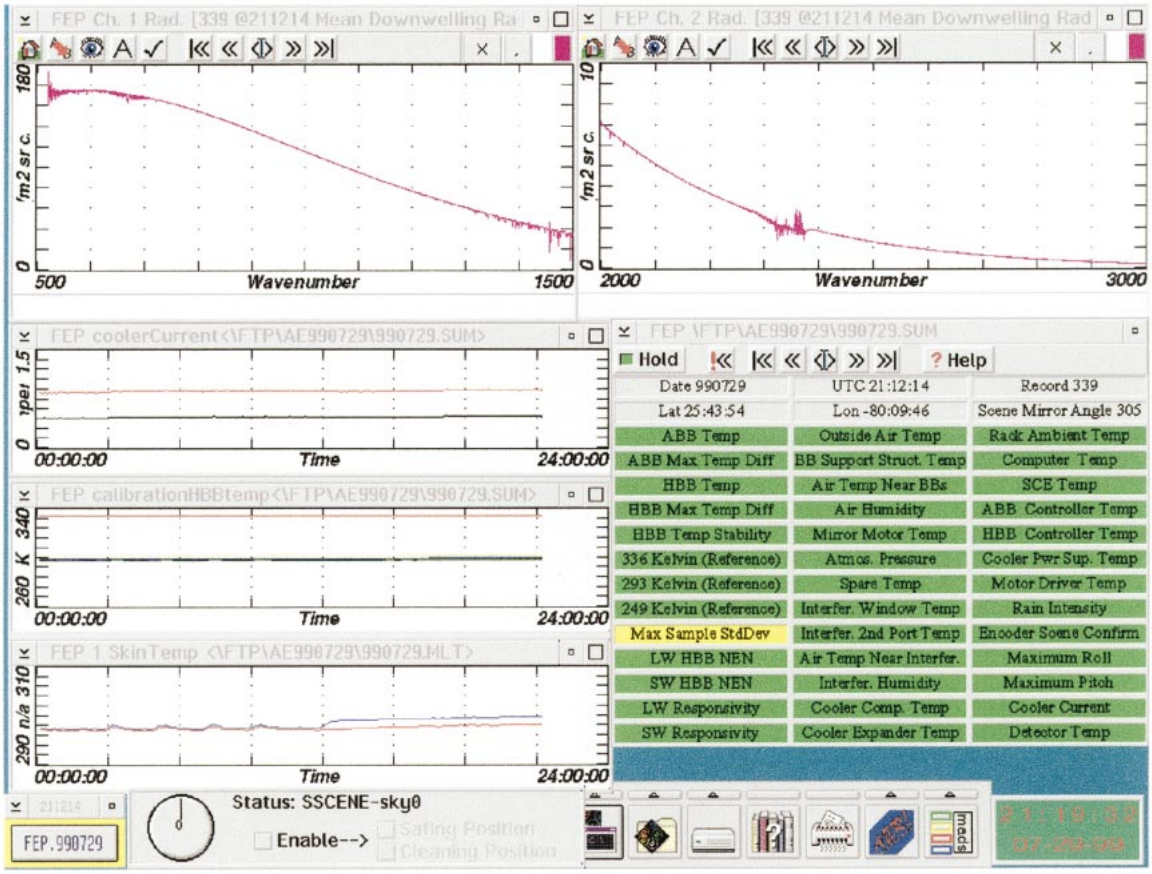

FIG. 6. An example of the display screen on the M-AERI computer. The most recent spectra are displayed in the top two panels (note change in vertical scale), and time series of relevant parameters are shown in the other graphs, including surface skin (red) and air (blue) temperatures (bottom left). The ''light box,'' showing the status of several critical parameters in a ''traffic light'' color code, is at the lower right. The M-AERI was operating in the laboratory when this screen was captured, so the spectra in the top panels, which are of downwelling radiation at a zenith angle of 55° (scene mirror angle 305°), are smooth (emission from the ceiling). The display was last updated at the completion of the most recent set of measurements at 2112:14 UTC. The time of the screen dump is 2119:32 UTC on 29 Jul 1999, as shown in the clock in the lower right corner, which shows the current time based on the GPS time signal. The instantaneous position of the scene mirror is shown by the display at the bottom, left of center, which indicates an upward-looking configuration measuring the incident radiation at zenith.

sample average). The merged data stream is recorded in a customized data format [descriptive multivariable (DMV) format] developed at the University of Wisconsin and is accessible through a library of C-language routines. After creation of the DMV format data files, a sequence of FORTRAN language modules are executed under the control of a REXX-based set of command scripts. A series of five processing steps are performed on the raw data (Fig. 8):

1) a correction for detector nonlinearity is applied to the long-wave (HgCdTe) band,
2) the forward and backward Michelson scans for each of the long-wave and short-wave bands are calibrated individually,
3) the forward and backward scans are averaged for each band,
4) a finite field of view correction is applied to each calibrated spectrum, and
5) the spectra are resampled to a ''standard'' wavenumber scale common to all M-AERI systems.

After the five processing steps, a separate application reviews the processed data and compiles a file of summary information, including instrument performance characteristics and data quality flags. The final processing step is the computation of the SST from a combination of calibrated ocean and sky views (see section 4b below). The final data products made available for archive are the uncalibrated raw data; the final calibrated, corrected, and resampled radiance observations; and the summary product file. Table 3 represents the data flow by giving the filename extensions as used to

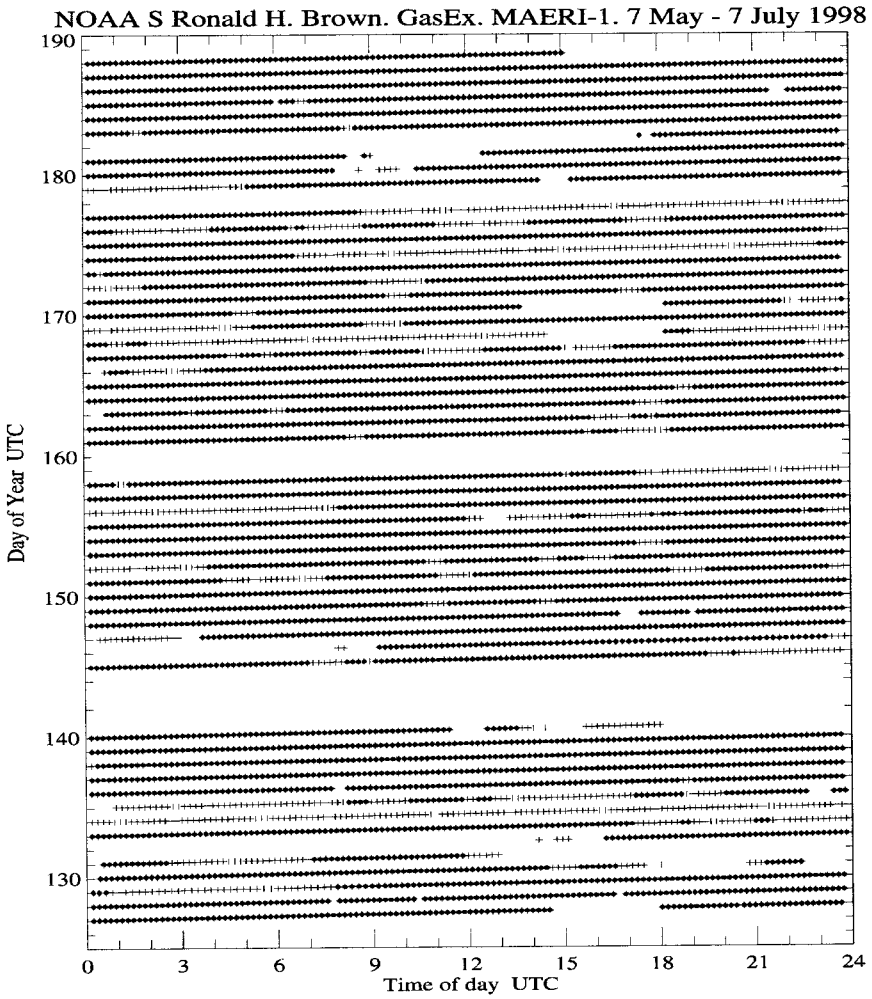

FIG. 7. An example of the rate of data return from the M-AERI during the ''GasEx'' cruise of the NOAA S *Ronald H. Brown* in the North Atlantic Ocean. Each dot indicates the time of measurements of an independently calibrated set of atmosphere and oceanic spectra, and the crosses indicate when the instrument was covered by a tarpaulin to protect against spray or heavy rain. Long gaps in the sequence indicate periods when the ship was in port or when scientific operations were shut down by a storm (days 159 and 160), and short gaps indicate where the data were lost as a result of maintenance (cleaning the scene mirror), automatic safing of the mirror in conditions of drizzle of light spray, or instrument problems (usually caused by loose cables or connectors). Such data losses comprise, in this example, 6.4% of the possible data return. Good data were collected for 78% of the total possible time.

indicate the intermediate and final data products produced by the real-time processing system.

e. Data display

An example of the data display on the monitor of the control computer is given in Fig. 6. The upper two panels show the most recently measured calibrated spectra for the two detectors, which are updated in real time. Previous spectra from the current day can be quickly recalled for comparison.

As described above, the M-AERI is equipped with a range of sensors that report on the state of the hardware. This is to assist the operator in monitoring the status of the instrument and data flow. The data acquisition software applies real-time quality-assurance checks to both the interferometer data stream and these ''housekeeping'' measurements. Several of the parameters are plotted in real time as time series on the screen of the control computer. Sudden displacements or slow trends in the time series plots are quite obvious, and the color changes in the warning lights, which occur when the specific measurements fall progressively outside preset thresholds going from green to yellow to red, are an immediate indication of possible data degradation. Catastrophic data loss, such as results from a cable break or a connector failure or by the internal temperature of the FTIR falling or rising outside of the operating range, triggers

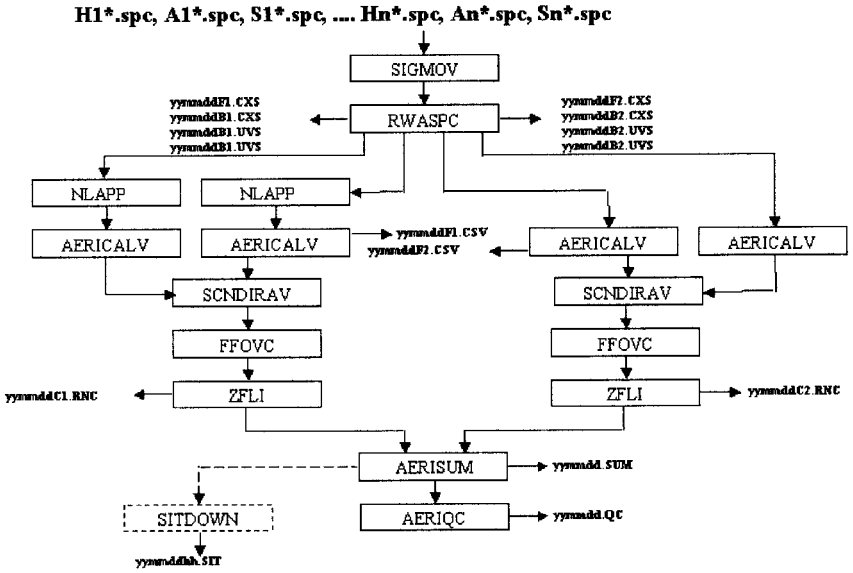

FIG. 8. Flow diagram of the data through the processing stream. (See also Table 4.)

audible as well as visual warnings to the operator. The screen also includes a display of the current mirror position and buttons to override the mirror sequence to immediately enter the mirror-safe mode or to position the mirror for cleaning.

f. Signal-to-noise

Tests have shown that the dominant source of noise in the system is that caused by the detectors themselves, and the target values of the noise equivalent radiance difference (NEΔL), given in Table 1, are for a single scene measurement over a 1-s interferogram. In reality, the NEΔLs for each set of detectors is somewhat below these target levels. The signal-to-noise ratio (SNR) is a function of position in the spectrum and the temperature of the target scene. For measurements of the sea surface, the typical radiance values range from $\sim$160 mW(m^2 sr cm^{-1})$^{-1}$ at $\sim$670 cm^{-1} (λ = 15 μm) to $\sim$35 mW(m^2 sr cm^{-1})$^{-1}$ at $\sim$1500 cm^{-1} (λ = 6.7 μm) to give SNRs of $\sim$800 to $\sim$175 for the long-wave (HgCdTe) detector for the target NEΔL. For the short-wave (InSb) detector, typical radiance values range from $\sim$7 mW(m^2 sr cm^{-1})$^{-1}$ at $\sim$2000 cm^{-1} (λ = 5 μm) to $\sim$0.3 mW(m^2 sr cm^{-1})$^{-1}$ at $\sim$3000 cm^{-1} (λ = 3.3 μm) to give SNRs of $\sim$467 to $\sim$20. Averaging over 45 independent interferograms, as is routinely done in at-sea operations, increases these numbers to $\sim$5400 to $\sim$1135 and $\sim$3135 to $\sim$135. At λ = 7.7 μm, used for the routine measurement of the skin SST (see section 4a below), typical radiance values are $\sim$55 mW(m^2 sr cm^{-1})$^{-1}$, leading to an SNR of $\sim$270 for a single interferogram and $\sim$1800 for a 45-s average.

The spectrum of the downwelling sky radiance is much more variable (Fig. 3), and in the spectral intervals where the atmosphere is very transparent and path lengths are long, is very dependent on the state of the atmosphere. In conditions of low cloud, the emission is similar to that from the sea surface, and the single scene SNRs given above are applicable. In routine operations, we average over 60 zenith-view interferograms, so the SNRs increase by a factor of 15%. For clear skies, these SNRs remain appropriate for the spectral intervals where path lengths are short but degrade with increasing atmospheric transmission and path length. In the extreme conditions of cold, dry atmospheres, the averaged

TABLE 3. MAERI processing data flow where FW/BW refers to the forward or backward Michelson scan and LW/SW = long-wave or short-wave detector band. Bold characters indicate the data files that are routinely archived.

Processing level	FW/LW	BW/LW	FW/SW	BW/SW
Raw data	**F1.CXS**	**B1.CXS**	**F2.CXS**	**B2.CXS**
Nonlinearity correction	F1.CXV	B1.CXV		
Calibration	F1.RLC	B1.RLC	F2.RLC	B2.RLC
Scan direction average	C1.RLC		C2.RLC	
Finite FOV correction	C1.RFC		C2.RFC	
Spectral resampling	**C1.RNC**		**C2.RNC**	
Summary		**.SUM**		
Sea surface temperature		**.MLT**		

SNRs can be <10 in spectral intervals where the path length is very long, such as ~1100 cm^{-1} (see Fig. 3).

g. Calibration

The calibration of the M-AERI system has two separate components: spectral and radiometric. The spectral calibration provides confidence in the position of features in the measured infrared spectra, and the radiometric calibration is necessary to determine the instrument's response function so that a quantitative relationship is established between the measurements and the incident radiative flux intensity and hence the temperature of the source of the radiation.

1) SPECTRAL CALIBRATION

The spectral calibration is done by making upward-looking measurements of the clear, cold sky, which provides spectra with well-defined atmospheric emission lines (e.g., Fig. 3). The positions of the lines in the measured spectra are compared with those in a library of atmospheric gas spectra to determine the effective wavelength of the internal HeNe laser and hence the FTIR's wavenumber sampling scale.

2) RADIOMETRIC CALIBRATION

The radiometric calibration of the M-AERI is done continuously throughout its use. As with simpler self-calibrating radiometers, an FTIR spectroradiometer can be calibrated by using two blackbody targets at known temperatures. These provide two reference spectra to determine the gains and offsets of the detectors and associated electronics. Since the instrument measures interferograms rather than spectra or spectrally integrated radiance (as is the case with a bandpass filter radiometer), it is important that the calibration be independent of the positions of the moving mirrors. This is achieved by very careful assembly, especially in position and alignment of the field stop, so that the effective aperture size and its projection onto the detectors is insensitive to path length differences. Further technical details of FTIR calibration are given by Revercomb et al. (1988).The mirror scan sequence includes measurements of both reference cavities before and after each set of spectra from the ocean and atmosphere.

The absolute accuracy of the infrared spectra produced by the M-AERI is determined by the effectiveness of the blackbody cavities as calibration targets, which in turn depend on their design, quality of construction, and calibration of the thermometers used to determine their temperatures (see above). The two fixed blackbody cavities are used in the routine calibration of the spectra and a third of identical construction is used periodically in the laboratory or the field to check the absolute calibration of the instrument. It is temporarily fixed so that its aperture captures the entire field of view of the M-AERI, and its temperature is varied in steps through the required range. Typical uncertainties in the retrieved temperature across the whole spectral range are <0.03 K (Fig. 9). To provide a calibration confirmation at lower than ambient temperatures, an ice bath is inserted into the field of view at nadir in the laboratory; typical uncertainties across the spectrum are <0.05 K. The mounting assembly for the blackbody cavities is such that the atmospheric path lengths from the FTIR entrance aperture to each of the blackbody apertures is the same.

A further independent determination of the M-AERI's absolute radiometric accuracy was made during an infrared radiometry workshop held at the Rosenstiel School of Marine and Atmospheric Science, University of Miami (RSMAS) in early 1998 (Kannenberg 1998). A water-bath blackbody calibration target (Fowler 1995) was provided by NIST, and a M-AERI was set up to measure its temperature at three set-point temperatures. The M-AERI was mounted so the axis of the scan mirror was at the same height as, and orthogonal to, the axis of the blackbody cone. The radiation entering the M-AERI was therefore emitted in a beam centered on the cone axis. The atmospheric path length was minimized by bringing the M-AERI as close to the NIST unit as the physical dimensions would allow, that is, about 20 cm from the cone aperture to the entrance window of the FTIR. The results are shown in Fig. 10, which shows the discrepancy between the M-AERI brightness temperature measurement and the NIST target at the three set points. The 20°C measurements were taken at close to ambient temperature in the laboratory and therefore are expected to produce the best correspondence, as is indeed the case. These represent the situation of the M-AERI sea surface measurements where the target is generally within a few degrees of the instrument temperature. As the temperature of the NIST blackbody target was increased, the discrepancies increased, but mainly by introducing a slight bias error that is consistent with the reflectance of stray, ambient-temperature radiation from a blackbody target with an emissivity less than unity. The results of the measurements in two clear parts of the spectrum, from each of the two detectors, are shown in Table 4.

The calibration of the M-AERI spectra taken under laboratory conditions is thus both stable and accurate. In the field, however, there are several factors that could lead to degradation of the data. These include wind cooling of the heated blackbody; contamination of the exposed optical surfaces by sea spray, rain, or ship exhaust depositions from the ships; or temperature-related effects as the instrument heats and cools through the diurnal temperature cycle. Confidence in the at-sea measurement is derived from the comparison between skin SST retrievals from two M-AERIs operating side-by-side. The results of these comparisons are discussed below.

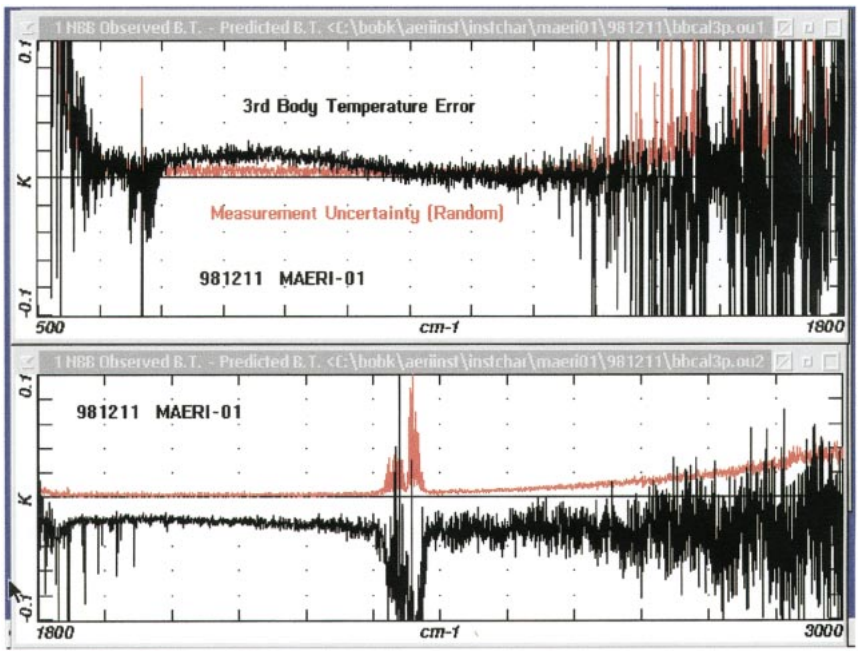

FIG. 9. An example of the ''3-body'' calibration in which the M-AERI measures the emission spectra from a third blackbody calibration cavity at a known temperature. The upper panel shows the spectrum of the temperature discrepancy from the HgCdTe detector (long-wave channel) and the lower from the InSb detector (short-wave channel). The noisy parts of the spectra are where the atmosphere is insufficiently transparent for the instrument to measure clean signals from the two blackbody cavities used in the calibration procedure. In the clear parts of the spectra, the measurement errors are typically 0.02 K or less. The skin temperature retrievals take place in at about 1300 cm^{-1}, in the long-wave channel, where the errors are <0.01 K.

3. At-sea deployments: R/V *Roger Revelle* cruise

In this section, we describe a deployment of two M-AERIs on the R/V *Roger Revelle* undertaking a quasimeridional section in the Pacific Ocean from Hawaii to New Zealand in the Northern Hemisphere autumn 1997 (28 September to 13 October). Two instruments were used in parallel to provide a database with which to assess the accuracy of the M-AERI measurements.

a. Cruise description

The R/V *Roger Revelle* sailed from the University of Hawaii Marine Facility in Honolulu for Lyttleton, New Zealand, at speeds of 10–12 knots (5–6 m s^{-1}). The cruise track (Fig. 10) crosses both Northern and Southern Hemisphere trade wind zones, the equatorial region including the Intertropical Convergence Zone, and the westerlies (''roaring forties'') of the Southern Hemisphere.

The two M-AERIs were mounted on the starboard side on the 02 deck, with M-AERI-01 being forward of M-AERI-02. Both were mounted high enough so that they viewed undisturbed water, ahead of the ship's bow wave, with a view angle of 45° and greater (measured from nadir). The separation of the fields of view of the two instruments at the sea surface was less than 2 m. The instruments' umbilical cables were run along the exterior of the ship into the main scientific laboratory two decks lower, where the computers and electronics interfaces were installed. The prevailing winds throughout the cruise, with the exception of the Southern Hemisphere westerlies, were from the port side of the ship, and the M-AERIs were in the lee of a crane on the 02 deck. During strong wind conditions, when the risk of salt spray entering the instruments was high, and during heavy rain, the M-AERIs were covered by tarpaulin sheets for protection, and no data were collected. Similarly, when there was evidence of direct sunlight entering the aperture, a shield was used, which obscured some of the environmental views at the affected mirror angles. Otherwise, the instruments were run continuously.

b. Parallel operations: M-AERI-01 versus M-AERI-02 SST retrievals

Prior to mounting on the R/V *Roger Revelle*, the calibrations of both M-AERIs were checked by measuring the temperature of a third blackbody target at a known temperature. Both M-AERIs measured the temperature of this target with uncertainties of <0.03 K.

The two sets of measurements are independent in the sense that each instrument has its own internal calibration. The two instruments have slightly different cycle

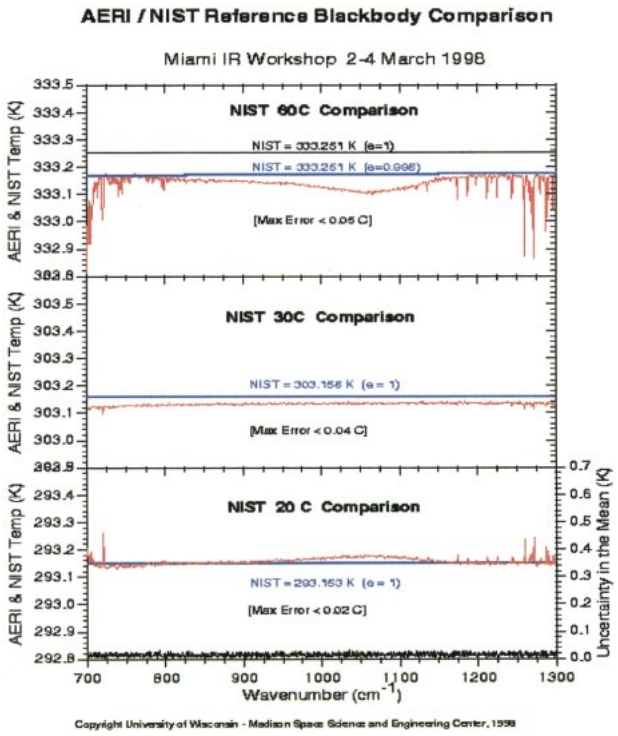

FIG. 10. The M-AERI brightness temperature spectra and NIST calibration target temperatures for three set-point temperatures, e being the emissivity of the blackbody cavity.

times, determined by the speed of the moving mirror in each interferometer, and thus it was impossible to synchronize the two datasets even when both instruments were using the same scan mirror control sequence. So to compare the skin SST retrievals, the time series from M-AERI-02 was interpolated to the measurement times of those from M-AERI-01. Daily averages of the differences in skin SSTs from both instruments are given in Table 5 together with their standard deviations. It can be seen that the correspondence is remarkably good and is better than anticipated given the design goals (<0.1 K) and what were believed to be the inherent uncertainties in key components of the instrument (e.g., emissivity of blackbody calibration targets; accuracy of the reference thermometers in the blackbody cavities). Impressive as these results are, they do not constitute a rigorous affirmation of the absolute accuracy of the instruments, as both instruments were built at the same laboratory and therefore share a common calibration history at the SSEC. Should the calibration of the reference thermometers have drifted from the NIST standard, the M-AERI measurements may still agree very well but would be in error on an absolute scale. However, taken in conjunction with the results from laboratory calibrations and the Miami workshop (discussed above), these inspire confidence in the M-AERI SST measurements at levels of uncertainty <0.1 K. A comprehensive comparison with SSTs derived from other well-calibrated radiometers at sea is underway.

TABLE 4. Laboratory tests of M-AERI accuracy. The mean discrepancies in the M-AERI 02 measurements of the NIST water-bath blackbody calibration target in two spectral intervals where the atmospheric absorption and emission are low. Discrepancies are M-AERI minus NIST water-bath blackbody temperatures.

Target temp.	LW (980–985 cm^{-1})	SW (2510–2515 cm^{-1})
20°C	+0.013 K	+0.010 K
30°C	−0.024 K	−0.030 K
60°C	−0.122 K	−0.086 K

4. Applications

The applications of the measurements of a well-calibrated FTIR, such as the M-AERI, are many and range from atmospheric spectroscopy (Mlawer et al. 1998) and meteorological profiling (Feltz et al. 1998) to SST retrieval (Smith et al. 1996). Here we present and discuss some examples related to the oceanographic applications for which the M-AERI was designed. These topics are reported in varying degrees of detail. In some cases, the discussion is focused on published work, and in others, it is limited to a brief discussion, as these are the subjects of continuing research, insufficiently mature for publication at present but nevertheless included here to indicate the richness of the information in the M-AERI spectral measurements.

a. SST measurements

In principle, the surface emission measured at any wavelength can be used to derive the SST, provided the atmosphere is sufficiently transmissive to allow a significant component of the sea surface emission to propagate through the path between the surface and the M-AERI aperture. However, there is another consideration in that the spectral variations in the infrared properties

TABLE 5. Discrepancies in skin SST measured by two M-AERIs on the R/V *Roger Revelle* section, Hawaii to New Zealand, 1997. Measurements at a 55° incidence angle, $\lambda = 7.7$ μm. The M-AERI-01 data are interpolated to the times of M-AERI-02 measurements. Statistics are calculated over 24-h data segments. The $\Delta_m T$ = Skin SST (M-AERI-02 minus M-AERI-01).

Date (UTC)	N	Mean $\Delta_m T$ K^{-1}	St dev $\Delta_m T$ K^{-1}
October 1	70	0.005	0.033
October 2	58	0.020	0.084
October 3	56	0.002	0.092
October 4	85	0.005	0.059
October 5	56	0.000	0.091
October 6	79	0.021	0.067
October 7	146	0.000	0.073
October 8	74	−0.003	0.085
October 9	133	0.009	0.062
October 10	133	−0.003	0.099
October 1–10	890	0.005	0.077

of seawater mean that there are sections of the spectrum where the emission comes from somewhat deeper (but still less than 0.5 mm depth) in the ocean than at other spectral intervals. Thus, since there are nearly always gradients in the skin layer of the ocean, the temperature derived from the spectra will depend on wavelength. This can be utilized to derive the temperature profile through the skin layer (see section 4e below), but for the retrieval of the interfacial temperature, measurements from spectral intervals must be used where the emission depth of the radiation is very shallow. This is the case for emission at infrared wavelengths of longer than about 5 μm (Friedman 1969).

The radiance measure by the M-AERI while viewing the sea surface is a combination of the radiation emitted at the surface and of incident radiation reflected at the surface. In addition, there is a component of radiation emitted by the atmosphere between the sea surface and the instrument; for a M-AERI mounted on a ship at a height of a few meters, this component is very much smaller than the others:

$$R_{\text{water}}(\lambda, \theta) = \varepsilon(\lambda, \theta)B(\lambda, T_{\text{skin}}) + (1 - \varepsilon(\lambda, \theta))R_{\text{sky}}(\lambda, \theta) + R_h(\lambda, \theta), \quad (1)$$

where $R_{\text{water}}(\lambda, \theta)$ is the calibrated radiance measurements made at a nadir angle θ and wavelength λ; $B(\lambda, T_{\text{skin}})$ is the sea surface emission at wavelength λ zenith angle θ and temperature T_{skin}; $R_{\text{sky}}(\lambda, \theta)$ is the downwelling atmospheric emission (including that from clouds or aerosols if present) at wavelength λ and zenith angle θ; $R_h(\lambda, \theta)$ is the atmospheric emission for the layer below the level of the instrument at height h, both direct and reflected at the sea surface, subsequently attenuated by the atmosphere between the surface and height h; and $\varepsilon(\lambda, \theta)$ is the sea surface emissivity at wavelength λ and emission angle θ. This formulation, where θ is common to all terms, assumes specular reflection at the sea surface. This is not necessarily the case in all but the calmest conditions. However, the reflectivity of the sea surface is $[1 - \varepsilon(\lambda, \theta)]$, and recent modeling studies (Watts et al. 1996; Wu and Smith 1997) have shown that the wind-speed dependence of the sea surface emissivity is smaller than shown in earlier studies (e.g., Masuda et al. 1988), so the approximation of specular reflection appears to be better than previously thought. The consequences of nonspecular reflection from the roughened sea surface can be reduced by a careful selection of the wavelength used in the measurement (see below).

The downwelling atmospheric emission, $R_{\text{sky}}(\lambda, \theta)$, is measured by directing the M-AERI field of view at the same angle with respect to zenith, as the sea-viewing measurement is made with respect to nadir. This produces a spectrum of atmospheric radiation down to the instrument level. The small correction for the layer of atmosphere between instrument and sea surface is done using a parameterization, derived by radiative transfer simulations (see Smith et al. 1996), based on the measured air temperature (see below) instrument height, and view angle.

Solving Eq. (1) for T_{skin} gives

$$T_{\text{skin}} = B^{-1}\langle\{R_{\text{water}}(\lambda, \theta) - [1 - \varepsilon(\lambda, \theta)]R_{\text{sky}}(\lambda, \theta) - R_h(\lambda, \theta)\}/\varepsilon(\lambda, \theta)\rangle. \quad (2)$$

The skin SST values are derived routinely using a narrow spectral interval at a wavelength of $\sim$7.7 μm (1302–1307 cm^{-1}) at a nadir angle of 55°. This spectral interval (identified by the red vertical bar in Fig. 3) was selected to reduce the dependence of the accuracy of the retrieved SST on the correction for the reflected sky radiance (Smith et al. 1996). As the sea surface becomes rough in response to the wind or swell, the assumption of specular reflection implicit in Eq. (1) becomes less realistic, with sky radiance being reflected into the beam from other parts of the sky. At this wavelength, the atmospheric path length is much shorter than in the clearer spectral region at 10–12 μm, where SST is usually measured by filter radiometers, and so the dependence on changes on the zenith angle of the reflected sky radiation is much smaller, by more than an order of magnitude, as is evidenced in the top panel of Fig. 3.

The 55° angle was chosen because it exhibits a small wind speed dependence of the emissivity (Wu and Smith 1997) and can be accommodated with reasonable ease by the structural geometry of most ships, giving the M-AERI an unobstructed view of the sea surface ahead of the bow wave. The value of the emissivity used in the skin SST retrieval at 55° and 7.7 μm is 0.962627, which was determined from M-AERI data. The surface emissivity is dependent on emission angle, becoming smaller for increasing angle, and with increasing angular dependency on larger emission angle. Thus the reflectivity of the sea surface increases with larger view angles with respect to nadir, and this introduces a dependency on the roll of the ship. However, because of the relatively short path length of the reflected sky radiance at this wavelength, compared to that of radiation in the much more transmissive parts of the atmospheric emission spectrum, the difference in the sea and sky temperatures is smaller, and the retrieved SST error is much less influenced by changes in the surface reflectivity, such as introduced by ship roll. This lack of dependence on the view angle can be seen in the lower panel of Fig. 3, where the spread of $\pm$10° about 55° (black to turquoise) is very much smaller, again by more than an order of magnitude, at λ = 7.7 μm compared to λ = $\sim$10 μm.

As an example of the M-AERI sea surface skin temperature measurements, a section from Hawaii to New Zealand is shown in Fig. 12. This section extends over more than 50° of latitude (Fig. 11), and, as stated above, traverses a number of different climatic regimes. The

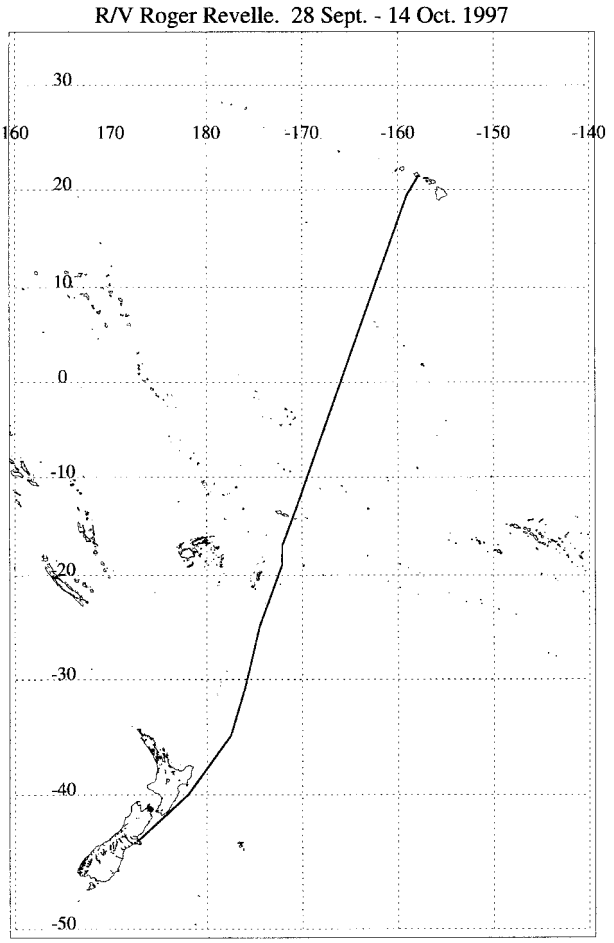

FIG. 11. Track of the R/V *Roger Revelle* on a transect from Hawaii to New Zealand.

upper panel of Fig. 12 shows the SSTs as measured by the M-AERI (colored line) and the ship's thermosalinograph at a depth of about 5 m (black line). The middle panel shows the difference between these two and the lower panel the true wind speed. The colors correspond to the local solar time and indicate the effect of diurnal warming in the upper ocean, which on calm days results in a positive difference between the skin and 5-m-deep temperatures, whereas in other cases, the skin is cooler. This is in accord with expectations based on consideration of the heat flux from ocean to atmosphere.

b. Emissivity

The presence of reflected sky emission in the sea-viewing data (Fig. 3) provides a mechanism for deriving the spectrum of the surface reflectivity and thereby also the surface emissivity; the two add to unity through Kirchhoff's law. [For a discussion of the application of Kirchhoff's law to the specific case of the sea surface emissivity, see the appendix of Wu and Smith (1997).] The spectrum of the surface reflectivity is expected to be a smoothly varying function and does not exhibit the line structure apparent in the atmospheric spectra. Therefore, the surface reflectivity spectrum can be derived by minimizing the local variance in a small spectral interval with respect to the fraction of the sky radiance spectrum removed from the sea surface radiance measurement. This approach was used by Smith et al. (1996) to derive estimates of the surface reflectivity and emissivity from the first cruise of the prototype M-AERI. The results were compared with the model predictions of Masuda et al. (1988) and were found to agree substantially, except in the case of large emission angles. Subsequent modeling by Watts et al. (1996) and Wu and Smith (1997) have shown the Masuda et al. (1988) model to overestimate the angular dependence of the emissivity at high emission angles, and by incorporating the effects of surface reflection of surface emission in rough seas, the theoretical emissivity spectra agree well with the measurements.

An example of M-AERI–derived sea surface emissivity is given in Fig. 13, which shows the wind speed dependency of surface emissivity at a wavelength of 3.7 μm. These data are from a 20-day cruise on the R/V *Melville* in waters around Baja, California, and 969 independent data points are shown. Also shown for comparison are the simulated emissivity values calculated by the models of Masuda et al. (1988) at emission angles of 50° (squares) and 60° (diamonds) and of Watts et al. (1996) at 55° (triangles). The M-AERI retrievals agree with the modeled values in a convincing fashion.

c. Air temperature

In those parts of the infrared spectra where the atmospheric path lengths are short (but not too short so that the radiance from the blackbodies does not reach the detectors, leading to calibration problems at these wavelengths), there is very little dependence of the radiance on view angle (upper panel of Fig. 3). These measurements are characteristic of the atmosphere close to the instrument. Air temperature is retrieved from the M-AERI spectra in the wavelength interval of 14.5–14.9 μm (670–690 cm^{-1}), designated by the vertical blue bars in Fig. 3. The temperature is characteristic of a distance of a few meters from the M-AERI aperture. Figure 14 shows a comparison between M-AERI–derived air temperatures and those measured by a conventional thermometer on the foremast of the NOAA S *Discoverer* in the tropical western Pacific during the Combined Sensor Cruise (Post et al. 1997). The mean difference is 0.10 K, with the M-AERI value being higher. The standard deviation is 0.22 K, of which about half can be ascribed to the M-AERI measurement.

The difference between the air and sea temperatures derived by the M-AERI is a good representation of the

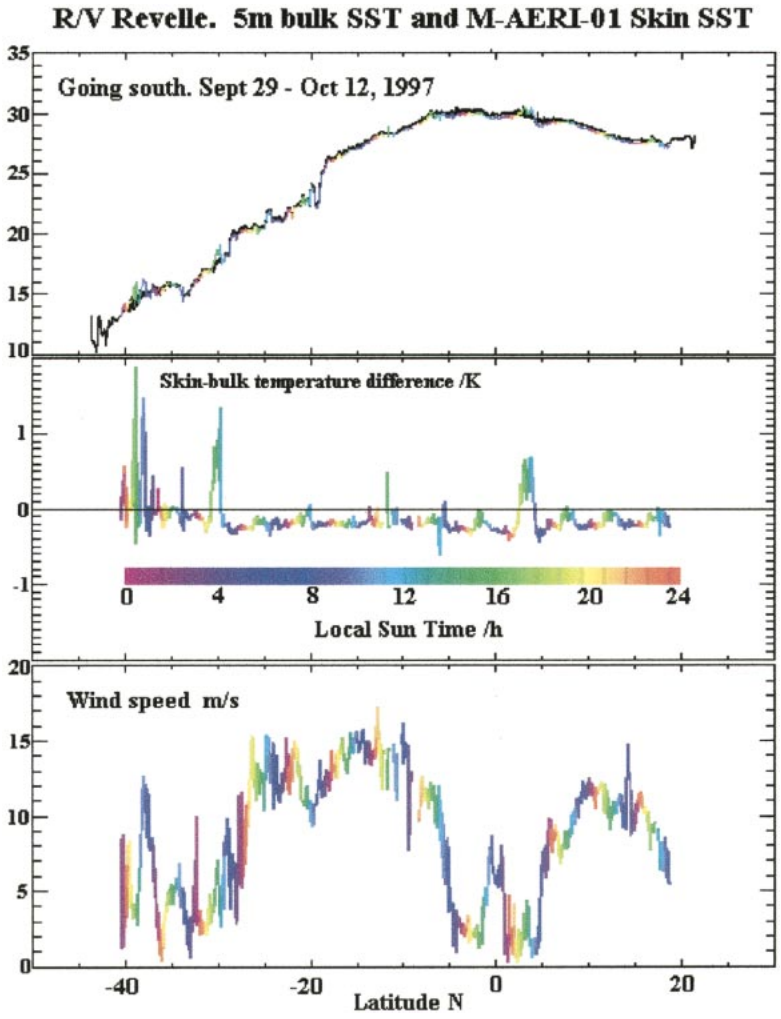

FIG. 12. The SSTs along the track of the R/V *Roger Revelle* (Fig. 11). The black line in the upper panel shows the measurements from the ship's thermosalinograph at a depth of about 5 m, and the colored line is the skin temperature derived from the M-AERI. The center panel shows the difference between the two. Wind speed, corrected for the effects of ship motion, is shown in the lower panel using the same color coding. The colors represent the local sun time for each measurement. The skin is generally a few tenths of a degree cooler than the bulk measurements, except in periods of low wind, when the development of diurnal thermocline gives the appearance of a warm skin layer.

true air–sea temperature difference because it uses the same sensor and calibration for both measurements. The conventional approach of using two thermometers introduces errors in the difference measurement from the uncertainties in the calibration of each sensor. On sunny days with low wind speed, the use of the M-AERI–derived skin SST also removes from the air–sea temperature difference measurement the influence of the near-surface temperature gradients that can occur between the depth of the bulk SST thermometer and the interface, and the radiometrically derived air temperature can reduce the influence of the heat-island effect of the ship. As an example, air–sea temperature differences measured close to the equator in the Pacific Ocean in June and July 1999 are -0.772 ± 0.566 K when determined by conventional instruments and -0.722 ± 0.113 K when measured by the M-AERI. The mean values are very close, but the radiometrically derived differences are much less variable, the discrepancies between the two time series being dominated by diurnal signals. In fact, the conventional measurement of air–sea temperature difference changed signs each afternoon as a result of the ship's heat island effect or inadequate shielding of the air-temperature thermometer against so-

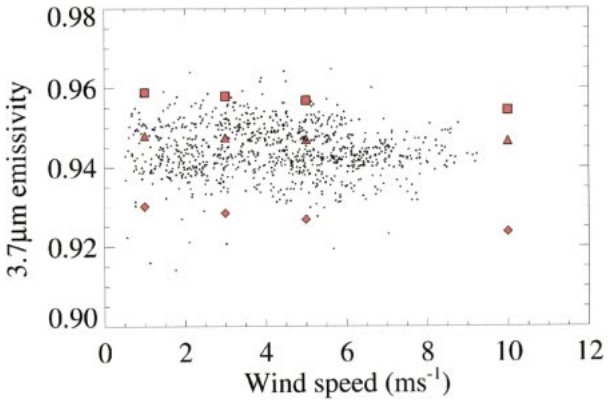

FIG. 13. Measurements of sea surface emissivity derived from M-AERI data in subtropical waters of Baja, California. The 969 individual emissivity retrievals, at a wavelength of 3.7 μm and an emission angle of 55°, are shown as a function of measured true winds. The symbols indicate the modeled values of emissivity according to Masuda et al. (1988) at an emission angle of 50° (squares) and 60° (diamonds) and to Watts et al. (1996) at 55° (triangles).

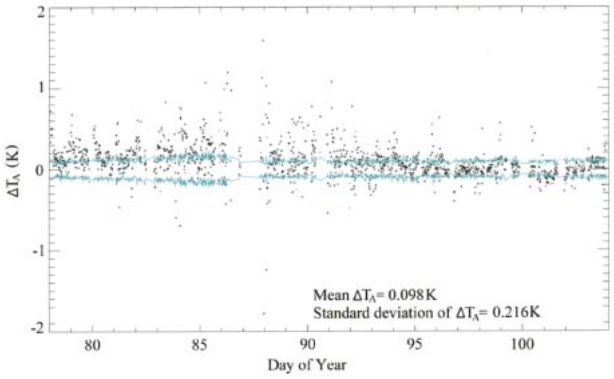

FIG. 14. Differences between the air temperatures derived from the M-AERI and a conventional thermometer. The ΔT_A is the difference between M-AERI–retrieved and conventionally measured air temperatures. The solid lines show the envelope of the standard deviations of the individual M-AERI air temperature retrievals. These are from the tropical western Pacific during the Combined Sensor Cruise Program from 18 Mar to 22 Apr 1996 (Post et al. 1997).

lar heating, whereas the radiometrically determined air–sea temperature difference remained negative (sea warmer than air) throughout.

d. Atmospheric profiles

The different effective atmospheric path lengths of the measured infrared spectra in the clear-sky zenith view means that the spectra contain information about the distribution and temperature of the gaseous constituents. These can be retrieved by using the spectra to invert the radiative transfer equation (Feltz et al. 1998; Smith et al. 1999). Although this is not yet regularly done with the marine atmosphere spectra from the M-AERI, it is now routinely accomplished with the AERI measurements from the southern Great Plains site of the ARM program (Stokes and Schwartz 1994). Temperature and humidity profiles are derived through the lowest 3 km of the atmosphere with a 10-min temporal resolution. Accuracies of the profiles when compared to radiosondes launched at the site are 0.6 to 1.3 K and 0.8 to 1.4 g kg^{-1} (Smith et al. 1999). Similar accuracies are anticipated for profiles through the lower marine atmosphere derived from M-AERI data. The retrieval of lower-tropospheric temperature and humidity profiles from the at-sea M-AERI spectra is a subject of active research and will be reported in a subsequent paper.

e. Skin temperature profiles

In an analogous fashion, the spectral variations of the optical path lengths through liquid water can be exploited to measure temperature gradients in the uppermost layer of the ocean. Throughout most of the spectral range of the M-AERI, such variations in the effective optical depth of water are very small indeed, being less than 25 μm. But in the interval defined by 3.3 μm $< \lambda <$ 4.3 μm, the effective optical depth has a maximum value of $\sim$65 μm. This means that spectral temperature variations can be mapped into a temperature gradient in the upper part of the thermal skin layer.

Making use of spectral temperature differences to determine the temperature gradient in the skin layer was proposed by McAlister and McLeish three decades ago (McAlister and McLeish 1969). They suggested using a two-channel filter radiometer with pass-bands centered in regions of differing optical depth. The application of this to continuous spectral measurements was demonstrated in the laboratory by McKeown et al. (1995) who, using a forerunner of the M-AERI, found good agreement between the measured gradients and those required by the known heat flux, determined by calorimetry of the target water bath. Additional confirmation that the measured gradients are credible is found in the fact that temperature measurements at wavelengths with the same effective optical depth are very similar. This causes an overlap at the gradients determined from the measurements on either side of the wavelength of maximum effective optical depth. McKeown et al. (1995) present results where the overlapping temperatures differ by less than 40 mK.

These measurements were made in the laboratory at values of heat flux somewhat greater than generally seen in the open ocean, and the extension of this approach to M-AERI measurements in oceanic conditions is the subject of continuing research (Hanafin and Minnett 2000). Initial analysis of cruise data has produced rather confusing results, with credible profiles in some cases but not in others. In an attempt to understand these, experiments were conducted in the open air using fresh water in an insulated water bath. The water was heated to promote convective heat loss to the atmosphere, and the added complication of a wind-roughened surface

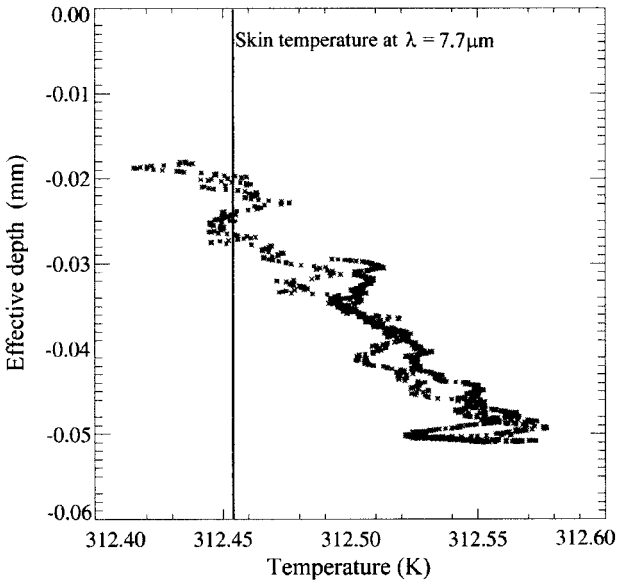

FIG. 15. Profiles of temperature measured through the skin layer of seawater measured in the 3.3 μm $< \lambda <$ 4.3 μm interval. The two profiles result from mapping the spectral information into depth into the skin layer going from shallow to deeper penetration, and then from deeper to shallower. The vertical line is the skin temperature derived from the spectra at ~7.7 μm (see section 4a). These measurements were taken in the open air, at night, with the water warmed to provide a heat flux to the atmosphere of ~700 W m^{-2}.

was kept to a minimum, as wind speed at no time exceeded 2 m s^{-1}. The measurements were made at night to avoid the issue of reflected sunlight in the short-wave infrared region. Preliminary results are encouraging (Fig. 15), with similar features as found by McKeown et al. (1995), specifically profiles that overlap at the level of <40 mK. These measurements were made with integrations over 110 interferograms for each spectrum of sea and sky emission. This profile was caused by a rate of heat loss of ~700 W m^{-2}, which is high compared to that found over much of the open ocean. Even though this result is encouraging, the application of this analysis to open ocean cruise data is still not guaranteed to produce useful information.

5. Discussion and conclusions

The Marine-Atmospheric Emitted Radiance Interferometer (M-AERI) is a seagoing Fourier-Transform Infrared Spectroradiometer that has now been used on several research cruises ranging from Arctic to equatorial conditions. It has been proven to be sufficiently robust to function at sea and take measurements in conditions where the temperature has ranged from −20 to +35°C and in wind speeds of up to ~17 m s^{-1}. At higher winds, the risk of spray contamination of the scene mirror causes the instrument to enter a safe mode, as is also the case in conditions of heavy rainfall. Much attention has been paid to ensuring a minimum of data loss during the routine operation of the M-AERI. Calibration can be maintained in the field to sufficient accuracy to study the skin effect (Hanafin and Minnett 2000) and validate satellite-derived SSTs (Kearns et al. 2000). The skin SSTs derived from the M-AERI spectra have residual uncertainties <0.1 K, and the comparison of M-AERI skin SSTs and AVHRR-derived SSTs yields discrepancies (~0.3 K) that are about half as large as previously published results. This is probably attributable to removing the effects of near-surface temperature gradients between the depth of a conventional in situ measurement and the sea surface, which are present in other comparisons but are absent when the M-AERI skin SST is used.

The M-AERI spectra can be used to derive air temperatures, which have residual uncertainties <0.3 K, when compared with conventional measurements from a nearby mast. The absolute accuracies of the M-AERI air temperatures are likely to be significantly better, as this figure includes the uncertainties of the conventional thermometer and real environmental variations between the two sensors. Thus for the first time, it is possible to measure the air–sea temperature differences with a single instrument. This removes the two largest sources of errors in this measurement: the calibration uncertainties of two separate thermometers and the near-surface temperature gradients in the water between the depth of the in situ water temperature measurements and the sea surface.

The high-resolution atmospheric emission spectra from the zenith-view M-AERI measurements contain information on the height and temperature distribution of the atmospheric gaseous constituents. These can be retrieved using the radiative transfer equation, and the derived atmospheric temperature and humidity profiles in the lower 2–3 km of the troposphere are credible when compared with radiosonde and Raman-lidar profiles. The accuracies with respect to radiosondes are in the range of 0.6 to 1.3 K for temperature and 0.8 to 1.4 g kg^{-1} for humidity (Smith et al. 1999). Again, the true accuracies of the retrievals are likely to be much better, as these values include uncertainties in the radiosonde measurements.

Similarly, temperature profiles in the thermal skin layer have been derived from the spectral information (McKeown et al. 1995) in laboratory conditions. Research is continuing with the objective of extending this approach to measurements in the open ocean, and a series of experiments conducted in the open using a water bath in partially controlled conditions have yielded some very encouraging results.

Current research using M-AERI data includes the study of the physical properties of the oceanic thermal skin layer (Hanafin and Minnett 2000) and its influence on air–sea exchanges, including those of CO_2 (Sikorski and Minnett 1999), the retrieval of atmospheric temperature and humidity profiles through the marine boundary layer and lower troposphere, and the valida-

tion of the SSTs derived by the AVHRR (Kearns et al. 2000), the ATSR, and the MODIS.

Acknowledgments. The robust nature of the M-AERI and high accuracy of the M-AERI spectra are the result of careful attention to detail by many members of the AERI group at the Space Science and Engineering Center, University of Wisconsin—Madison, especially Ralph Dedecker, Tim Dirkx, Ray Garcia, Hank Revercomb, John Short, and Bill Smith (now at NASA Langley Research Center). The captains, officers, and crews of the ships that have hosted the M-AERI are acknowledged for their at-sea support.

NASA funded the development of the M-AERI, through contract NAS5-31361 to O. B. Brown, and also supported much of the work reported here. Some of the fieldwork and analysis has been supported by NASA grant NAG56577 and by the DOE ARM program through grant 35249-AQ5, both to P. J. Minnett. The DOE ARM program also funded much of the development of the AERI.

REFERENCES

Donlon, C. J., and I. S. Robinson, 1997: Observations of the oceanic thermal skin in the Atlantic Ocean. *J. Geophys. Res.,* **102,** 18 585–18 606.

Esaias, W. E., and Coauthors, 1998: An overview of MODIS capabilities for ocean science observations. *IEEE Trans. Geosci. Remote Sens.,* **36,** 1250–1265.

Feltz, W. F., W. L. Smith, R. O. Knuteson, H. E. Revercomb, H. M. Woolf, and H. B. Howell, 1998: Meteorological applications of temperature and water vapor retrievals from the ground-based Atmospheric Emitted Radiance Interferometer (AERI). *J. Appl. Meteor.,* **37,** 857–875.

Fowler, J. B., 1995: A third generation water bath based blackbody source. *J. Res. Natl. Inst. Stand. Technol.,* **100,** 591–599.

Friedman, D., 1969: Infrared characteristics of ocean water (1.5–15 μm). *Appl. Opt.,* **8,** 2073–2078.

Griffiths, P. R., and J. A. de Haseth, 1986: *Fourier Transform Infrared Spectrometry.* Vol. 83, *Chemical Analysis,* John Wiley and Sons, 656 pp.

Hanafin, J. A., and P. J. Minnett, 2000: Profiling temperature in the sea surface skin layer using FTIR measurements. *Gas Transfer at Water Surfaces, Geophys, Monogr.,* Amer. Geophys. Res., in press.

Kannenberg, R., 1998: IR instrument comparison workshop at the Rosenstiel School of Marine and Atmospheric Science (RSMAS). *Earth Observer,* **10,** 51–54.

Katsaros, K., W. T. Liu, J. A. Businger, and J. E. Tilman, 1977: Heat transport and thermal structure in the interfacial boundary layer measured in a open tank of water in turbulent free convection. *J. Fluid Mech.,* **83,** 311–335.

Kearns, E. J., J. A. Hanafin, R. H. Evans, P. J. Minnett, and O. B. Brown, 2000: An independent assessment of Pathfinder AVHRR sea surface temperature accuracy using the Marine-Atmosphere Emitted Radiance Interferometer (M-AERI). *Bull. Amer. Meteor. Soc.,* **81,** 1525–1536.

Mammen, T., and N. von Bosse, 1990: STEP-A temperature profiler for measuring the oceanic thermal boundary layer at the ocean–air interface. *J. Atmos. Oceanic Technol.,* **7,** 312–322.

Masuda, K., T. Takashima, and Y. Takayama, 1988: Emissivity of pure and sea waters for the model sea surface in the infrared window region. *Remote Sens. Environ.,* **24,** 313–329.

McAlister, E. D., and W. McLeish, 1969: Heat transfer in the top millimeter of the ocean. *J. Geophys. Res.,* **74,** 3408–3414.

McKeown, W., F. Bretherton, H. L. Huang, W. L. Smith, and H. L. Revercomb, 1995: Sounding the skin of water: Sensing air–water interface temperature gradients with interferometry. *J. Atmos. Oceanic Technol.,* **12,** 1313–1327.

Minnett, P. J., 1995: The along-track scanning radiometer: Instrument details. *Oceanographic Applications of Remote Sensing,* M. Ikeda and F. Dobson, Eds., CRC Press, 461–472.

Mlawer, E. J., S. A. Clough, P. D. Brown, and D. C. Tobin, 1998: Collision-induced effects and the water vapor continuum. *Eighth Atmospheric Radiation Measurement (ARM) Science Team Meeting,* Tucson, AZ, U.S. Dept of Energy, Office of Energy Research, Office of Health and Environmental Research, Environmental Sciences Division, 503–511.

Mutlow, C. T., D. T. Llewellyn-Jones, A. M. Závody, and I. J. Barton, 1994: Sea-surface temperature measurements by the Along-Track Scanning Radiometer (ATSR) on ESA's ERS-1 Satellite—Early results. *J. Geophys. Res.,* **99,** 22 575–22 588.

Post, M. J., and Coauthors, 1997: The combined sensor program: An air–sea science mission in the central and western Pacific Ocean. *Bull. Amer. Meteor. Soc.,* **78,** 2797–2815.

Revercomb, H. E., H. Buijs, H. B. Howell, D. D. LaPorte, W. L. Smith, and L. A. Sromovsky, 1988: Radiometric calibration of IR Fourier transform spectrometers: Solution to a problem with the High Resolution Interferometer Sounder. *Appl. Opt.,* **27,** 3210–3218.

Schluessel, P., H.-Y. Shin, W. J. Emery, and H. Grassl, 1987: Comparison of satellite-derived sea-surface temperature with in-situ skin measurements. *J. Geophys. Res.,* **92,** 2859–2874.

Sikorski, R. J., and P. J. Minnett, 1999: Skin SST and air temperature measurements using a spectral IR interferometer (M-AERI). *Spring 1999 Meeting of the AGU,* Boston, MA, Amer. Geophys. Union.

Smith, W. L., and Coauthors, 1996: Observations of the infrared radiative properties of the ocean—Implications for the measurement of sea surface temperature via satellite remote sensing. *Bull. Amer. Meteor. Soc.,* **77,** 41–51.

——, W. F. Feltz, R. O. Knuteson, H. E. Revercomb, H. M. Woolf, and H. B. Howell, 1999: The retrieval if planetary boundary layer structure using ground-based infrared spectral measurements. *J. Atmos. Oceanic Technol.,* **16,** 323–333.

Stokes, G. M., and S. E. Schwartz, 1994: The Atmospheric Radiation Measurement (ARM) program: Programmatic background and design of the cloud and radiation test bed. *Bull. Amer. Meteor. Soc.,* **75,** 1201–1221.

Watts, P., M. Allen, and T. Nightingale, 1996: Sea surface emission and reflection for radiometric measurements made with the along-track scanning radiometer. *J. Atmos. Oceanic Technol.,* **13,** 126–141.

Wick, G. A., W. J. Emery, L. H. Kantha, and P. Schlussel, 1996: The behavior of the bulk-skin sea surface temperature difference under varying wind speed and heat flux. *J. Phys. Oceanogr.,* **26,** 1969–1988.

Wu, X., and W. L. Smith, 1997: Emissivity of rough sea surface for 8–13 μm: Modeling and verification. *Appl. Opt.,* **36,** 2609–2619.